InGaAs quantum dot chains grown by twofold selective area molecular beam epitaxy

Clément Barbot, Claire Rondeau-Body, Christophe Coinon, Yves Deblock, Pascal Tilmant, François Vaurette, Dmitri Yarekha, Maxime Berthe, L. Thomas, Heinrich Diesinger, et al.

▶ **To cite this version:**

Clément Barbot, Claire Rondeau-Body, Christophe Coinon, Yves Deblock, Pascal Tilmant, et al.. InGaAs quantum dot chains grown by twofold selective area molecular beam epitaxy. Nanotechnology, 2024, 35 (39), pp.395302. 10.1088/1361-6528/ad5f34 . hal-04752938

HAL Id: hal-04752938
https://hal.science/hal-04752938v1

Submitted on 25 Oct 2024

HAL is a multi-disciplinary open access archive for the deposit and dissemination of scientific research documents, whether they are published or not. The documents may come from teaching and research institutions in France or abroad, or from public or private research centers.

L'archive ouverte pluridisciplinaire **HAL**, est destinée au dépôt et à la diffusion de documents scientifiques de niveau recherche, publiés ou non, émanant des établissements d'enseignement et de recherche français ou étrangers, des laboratoires publics ou privés.

InGaAs quantum dot chains grown by twofold selective area molecular beam epitaxy

Clément Barbot, Claire Rondeau-Body, Christophe Coinon, Yves Deblock, Pascal Tilmant, François Vaurette, Dmitri Yarekha, Maxime Berthe, Louis Thomas, Heinrich Diesinger, Pierre Capiod, Ludovic Desplanque, Bruno Grandidier*

Univ. Lille, CNRS, Centrale Lille, Univ. Polytechnique Hauts-de-France, Junia-ISEN, UMR 8520 - IEMN, F-59000 Lille, France

E-mail: bruno.grandidier@univ-lille.fr

Received xxxxxx
Accepted for publication xxxxxx
Published xxxxxx

Abstract

Increasing quantum confinement in semiconductor quantum dot systems is essential to perform robust simulations of many-body physics. By combining molecular beam epitaxy and lithographic techniques, we developed an approach consisting of a twofold selective area growth to build quantum dot chains. Starting from 15 nm-thick and 65 nm-wide in-plane $In_{0.53}Ga_{0.47}As$ nanowires on InP substrates, linear arrays of $In_{0.53}Ga_{0.47}As$ quantum dots were grown on top, with tunable lengths and separations. Kelvin probe force microscopy performed at room temperature revealed a change of quantum confinement in chains with decreasing quantum dot sizes, which was further emphasized by the spectral shift of quantum levels resolved in the conduction band with low temperature scanning tunneling spectroscopy. This approach, which allows the controlled formation of 25 nm-thick quantum dots with a minimum length and separation of 30 nm and 22 nm respectively, is suitable for the construction of scalable fermionic quantum lattices.

Keywords: Selective area epitaxy, semiconductor nanowire, quantum dot chain

1. Introduction

Electron localization in a lattice is essential for the ongoing development of quantum systems, which aim at solving interacting fermionic problems. It can be achieved with semiconductor quantum dots (QDs) in which the restriction of the electron motion leads to a discrete atom-like electronic structure [1]. The most popular route to create QDs consists in electrically tuning the potential landscape of a two-dimensional (2D) electron gas [2,3]. Using remote gate voltages, linear and two-dimensional arrays of QDs have been defined in GaAs/AlGaAs or Si/SiGe heterostructures with an electrostatic disorder small enough to explore quantum coherence or perform quantum simulation and information processing [4,5,6]. Although the typical energies of the interdot coupling and the charging energy are weak, in the range of 100 μeV and 1 meV respectively, and would deserve to be increased for improved temperature accessibility, questions remain about the scalability of these systems with a limited number of control lines [7].

Alternatives to electrostatically designed arrays of QDs exist. For example, arrays of QDs can be obtained by the morphological instability of strained epi-layers. Using molecular beam epitaxy (MBE), an in-plane self-assembly of QD chains was demonstrated for increasing numbers of stacked InGaAs/GaAs multilayers [8,9]. More recently, 2D arrays of QDs were created with lithographic techniques by nanoperforating an $In_{0.53}Ga_{0.47}As$ semiconductor quantum

 © xxxx IOP Publishing Ltd

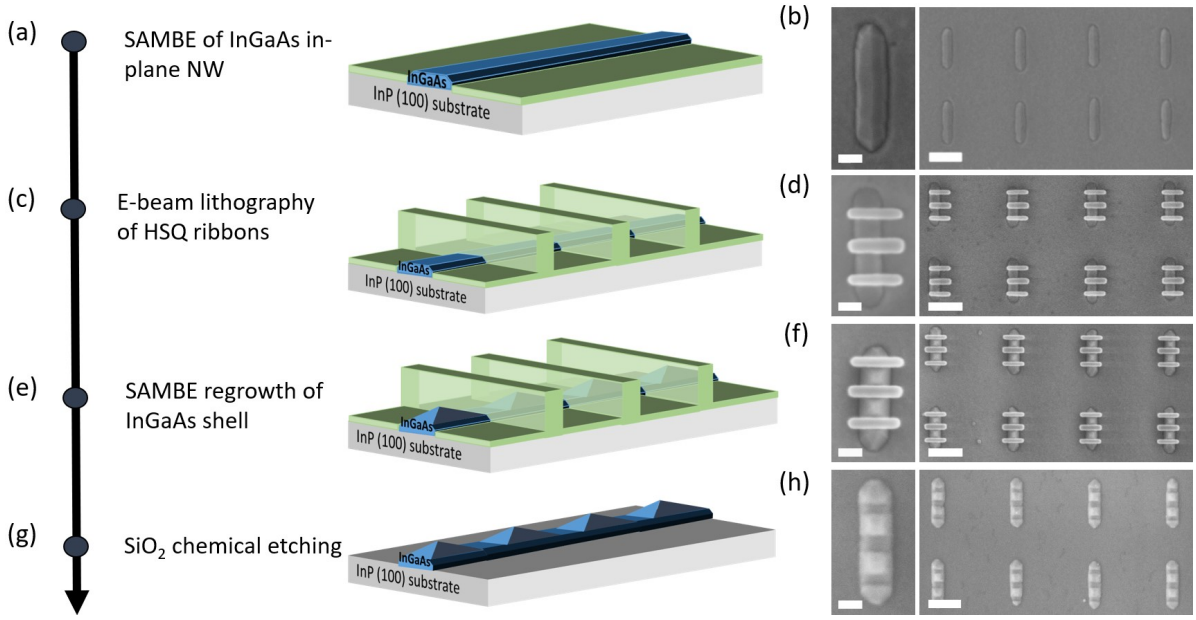

Figure 1. Experimental scheme for the fabrication of InGaAs QD chains based on multiple selective area molecular beam epitaxy (SAMBE) with corresponding SEM illustrations obtained after each step. (a-b) Selective area molecular beam epitaxy of an InGaAs NW in the opening of a SiO2 dielectric mask deposited on an InP (100) substrate. (c-d) Fabrication of HSQ nanoribbons defined by e-beam lithography across the InGaAs NW. (e-f) Selective area molecular beam epitaxy of InGaAs QDs on the InGaAs NW. (g-h) Removal of the HSQ and SiO2 dielectric mask to recover a clean surface for the subsequent characterization of the InGaAs QD chain with scanning probe microscopy. Scale bars: 50 nm (left), 200 nm (right).

well lattice matched to InP [10,11]. In both cases, the QD height is smaller than 10 nm and the circular base showed a diameter of about 35 nm. Such a geometry leads to a stronger quantum confinement with respect to the gate-defined QDs, somewhat relaxing the temperature constraint of the transport experiments. However, the QDs suffer from small fluctuations in size, which induces localization of the electrons in the biggest QDs, preventing the study of many-body physics.

Here, we aim at taking advantage of selective area growth, that relies on the combined use of MBE and lithographic techniques, to obtain an improved control over the QD size in linear arrays. Our scheme is based on the selective area epitaxy of in-plane semiconductor nanowires (NWs). While the NWs are created into a pattern transferred from a dielectric mask, the inhibition of the growth on the dielectric mask enables the fabrication of scalable and complex planar interconnected structures suitable for the transfer of quantum information [12,13,14,15,16]. By repeating the selective area epitaxy process on the NWs, we show the fabrication of $In_{0.53}Ga_{0.47}As$ QD chains on InP, where the vertical confinement is defined by the growth and, the lateral one by the dimensions of the patterned mask. As finding nanometer scale chains with scanning probe microscopies (SPM) is a tedious task, we designed a device layout for the navigation of the SPM probes. The variation of quantum confinement in the chains was then examined with kelvin probe force microscopy (KPFM) at room temperature and scanning tunneling spectroscopy at 77 K. The study of chains, for which the length of the QDs steadily decreases, reveals an increase of the quantum confinement, clearly discernible for the conduction band.

2. Selective area epitaxy of quantum dot chains

In-plane InGaAs QD chains, lattice-matched to InP, were fabricated using a two-step selective area molecular beam epitaxy (SAMBE) as described in figure 1. For the first step, a SiO_2 dielectric mask consisting of elongated openings or more complex opening networks was prepared on a Zn-doped InP(100) substrate by means of plasma-enhanced chemical vapour deposition (PECVD), e-beam lithography and reactive ion etching [17]. After a final hydrofluoric acid dip that fully opened the mask, the elongated openings exhibited a width of about 65 nm and lengths ranging from 300 nm to 3 µm. The sample was then outgassed for one hour at 180°C under ultra-high vacuum (UHV) before being transferred to the MBE system. The surface in the openings was deoxidized by a soft thermal annealing, below 500°C, under As_4 flux combined with a short exposure to an atomic hydrogen flux produced by a RF plasma cell during the temperature rise. A thin layer of InGaAs was then deposited in the openings with a nominal thickness of 10 nm at a temperature of 490°C and a growth rate of 0.2 monolayer per second (ML/s) with an As/In flux ratio of 5 (figure 1(a)). To ensure a good selectivity with respect to the oxide mask, the growth took place under an atomic hydrogen flux, resulting

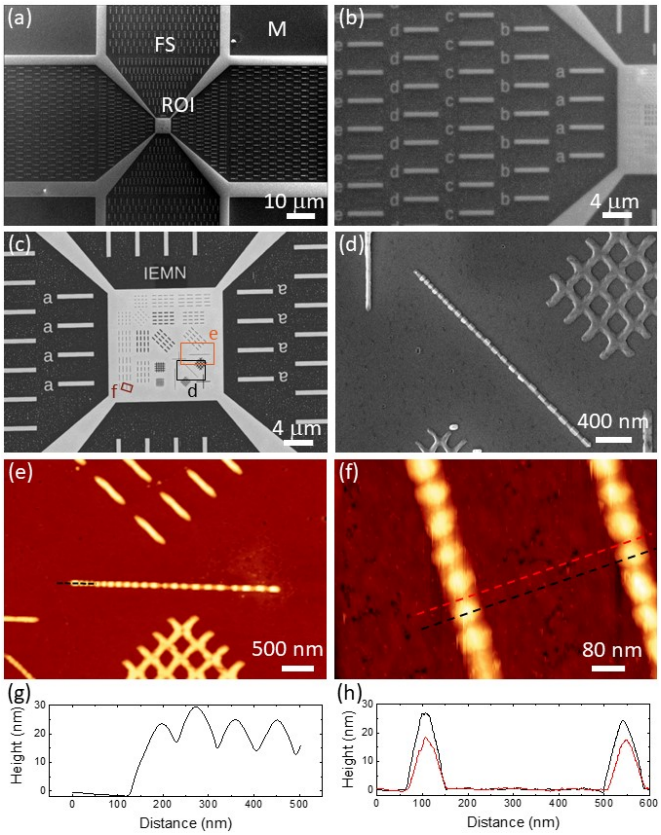

Figure 2. (a-c) SEM images with increasing magnification of the area surrounding the QD chains for an efficient navigation of the probe. One of the four markers, funnel shapes and the region of interest are labelled M, FS and ROI respectively. Three specific areas in the ROI, highlighted in (c), corresponds to (d) a SEM image and (e) an AFM image of a QD chain with QD lengths decreasing towards the centre of the ROI, (f) a STM image of two QD chains with QDs of similar sizes. The AFM and STM images were respectively obtained in ambient conditions and in UHV at 77 K. Feedback parameters for the STM image: V_s = +2.2 V, I_t = 564 pA. (g) and (h) Height profiles acquired along the dashed segments indicated in (e) and (f) respectively.

in the formation of $In_{0.53}Ga_{0.47}As$ nanowires, lattice-matched to InP [18], without any visible clusters on the dielectric mask, as shown in figure 1(b).

Localized overgrowth on the in-plane InGaAs nanowires was then performed using a hydrogenosilsesquioxane (HSQ) mask [19]. HSQ was spin coated with a thickness of 80 nm and then exposed to electrons. The unexposed areas were dissolved with TetraMethylAmmonium Hydroxide (TMAH) to leave a periodic array of HSQ ribbons across the InGaAs nanowires, as seen in figures 1(c) and (d). In these examples, the width of the ribbons varied between 30 and 40 nm. After outgassing the sample at 200°C in UHV, the surface of the InGaAs nanowires was deoxidized in the MBE growth chamber and a nominal thickness of 10 nm was deposited again with the same growth conditions as the ones used for the nanowire (figure 1(e)). As a result, InGaAs pyramidal shapes are obtained on top of the InGaAs nanowires in the spacing between the HSQ ribbons, as observed in figure 1(f). This image shows a good selectivity during the growth, since the number of parasitic clusters seen on the mask is small. After the growth, the HSQ ribbons and the SiO_2 dielectric mask were removed with a hydrofluoric-based chemical etching to leave chains of InGaAs QDs protruding out of the clean InP (100) surface (figure 1(g-h)).

Investigation of the QD chains with SPM requires to pre-pattern markers that guide the positioning of the probe over the region of interest (ROI) containing the chains. The ROI has a limited square size of 8 µm in width. To be able to locate it, it was designed in the centre of a 340 µm-wide square, defined at its corner by four square cavities, 100 µm in size. The four cavities, etched in InP with a depth of 200 nm, are readily observed with an optical camera and help to position the probe in the 140 µm-wide central region. Because this area is larger than the maximum scanning area of atomic force microscopy (AFM) and scanning tunneling microscopy (STM), an additional structure was designed around the ROI to guide the navigation of the probe more precisely. As seen in figure 2(a), it consists of four funnel shapes, all pointing towards the ROI. They were patterned and opened in the SiO_2 dielectric mask concomitantly with the NWs and QD chains, so that SAMBE also occurred in the funnel shapes. They encompassed small and periodic SiO_2 regions which defined segments, figures and letters used as landmarks for the navigation of the probes (figures 2(b) and (c)). To make the navigation easier, the letters and figures were rotated by 90° from a funnel shape to the next one. The position of the segments with respect to the letters (either on the left or on the right of the letters) indicates the direction to take to reach the ROI. The removal of the SiO_2 layer after the second growth left a bare InP surface in the ROI between the QD chains, around the InGaAs funnel shapes and in the segments, figures and letters of the funnel shapes. This difference of material composition is directly captured by the SEM images of figure 2, where the InP surface, 20 nm deeper than the InGaAs surface, appears bright.

For the analysis of the samples with SPM, a few samples were left in air to be characterized with a D3100 atomic force microscope and a NS4 controller (Bruker) in ambient conditions. Otherwise, they were loaded back to the MBE system to be cleaned and fully deoxidized with an atomic hydrogen flux exposure and a 400°C annealing under As_4 flux. They were subsequently exposed, at a temperature of 10°C, to an arsenic flux for 10 minutes. Capping the samples with such an amorphous arsenic layer efficiently protects their surface from air exposure and allows their transfer to a UHV system hosting a low-temperature scanning tunneling microscope (Omicron). Prior to the STM characterization, the As capping layer was removed by annealing the samples

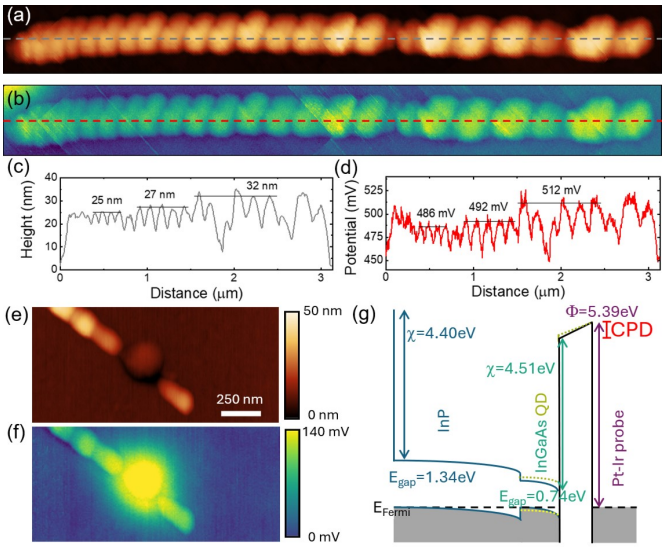

Figure 3. Room temperature (a) AFM and (b) KPFM images acquired simultaneously on a QD chain with QD lengths decreasing towards the centre of the ROI. The observed distortion from a straight chain is an experimental artefact caused by the drift of the scanner. The dashed lines indicate the position of the (c) height and (d) potential profiles. (e) AFM and (f) KPFM images acquired simultaneously on a QD chain with a missing QD. (g) Energy band diagram where the work function Φ of the Pt-Ir probe, the affinities χ and the band gaps E_{gap} of bulk InP and InGaAs are indicated. The change of the band position and bending with quantum confinement, and the resulting difference in contact potential (CPD) are highlighted with dotted lines.

at 350 °C, while monitoring the As desorption with mass spectroscopy [20].

Using an optical camera and operating the AFM tip in the tapping mode, the ROI was located within a few minutes. The AFM image in figure 2(e) shows the end of the tilted QD chain visible in the SEM image of figure 2(d) and another horizontal QD chain, both structures being separated by a 4x4 grid. While a height difference of 20 ± 4 nm is typically measured between the funnel shapes and the ROI, consistent with the nominal thickness of the InGaAs layer, the height profile of the QD chain indicates that the dots have a height higher than the nominal thickness, some of them reaching more than 30 nm (figure 2(g)). A similar increase of the height with respect to the total nominal thickness of InGaAs is also found for other QD chains located at the right bottom side of the ROI and imaged with STM (figure 2(f) and (h)). We attribute this deviation to the faceting of the QDs, which leads to a three-dimensional growth. We note that the width of the QD chains measured in the SEM images, 66 ± 1 nm, matches the width of the initial opening in the SiO_2 dielectric mask, indicating that the growth develops vertically and does not extend laterally. In contrast to the almost constant separation between the QDs seen in figure 1, tuning the width of the HSQ ribbons allowed to vary the QD separation. For the long QD chains visible in figures 2(d) and (e), where the width of sets of HSQ ribbons (triplet, quadruplet and even quintuplet) were steadily varied from 100 down to 20 nm by step of 10 nm, the minimum separation between two adjacent QDs was 25 ± 1 nm. Beyond this lowest limit, the growth is often impeded because of the partial development of the HSQ resist. Similarly, the length of the QDs was tuned between 90 nm and 30 nm. As a result, the smallest QDs had a minimum length of 30 nm, corresponding to the intended patterned length, while the minimum height was 22 ± 1 nm.

3. Quantum confinement in the quantum dot chains

To assess any change of confinement between the QDs, the QD chains were studied with KPFM in amplitude modulation lift mode at room temperature. This technique measures the contact potential difference (CPD) between a sample and a conductive AFM probe. When quantum size effects occur in a semiconductor QD, the number of charge carriers transferred into the QD from the substrate varies with the confinement. As a result, the surface potential measured on the QDs changes and can be mapped out by the measurement of the CPD [21]. Figure 3(a) shows an AFM image of a whole QD chain. Although the apostrophe shape of each QD is a probe artefact and the slight bending of the chain is caused by the drift of the instrument, this measurement provides series of reproducible QD heights along the chain. Three sets of QDs are observed from the left to the right with respective heights of 25 nm, 27 nm and 32 nm (figure 3(c)). The simultaneously acquired KPFM image (figure 3(b)) shows a clear contrast variation between the smallest QDs and the biggest ones. We rule out the origin of this variation to the topography because a missing dot, corresponding to a depression in the AFM image of figure 3(e), has a KPFM contrast brighter than the one observed on the adjacent QDs (figure 3(f)). Instead we attribute a higher CPD to residual charges at the position of the depression [22].

To further ensure that the change of CPD is meaningful, the difference of surface potential between the InP surface and the biggest QDs having the weakest quantum confinement is first analysed. The CPD is equal to the difference between the work function of the AFM probe and the work function of the sample divided by the elementary charge. The affinity of InP has been well established, 4.40 eV [23]. For p-type InP substrates covered with a native oxide layer, the Fermi level at the surface is known to be pinned 0.50-0.60 eV below the conduction band [24,25], yielding a work function of 4.95 ± 0.05 eV. The affinity of $In_{0.53}Ga_{0.47}As$, obtained from a Vegard's law interpolation between the affinities of GaAs and InAs, is 4.51 eV. Therefore, a positive CPD increase by 65 mV indicates a slightly lower work function for $In_{0.53}Ga_{0.47}As$, with a Fermi level pinned below midgap at the InGaAs surface (figure

3(g)). This pinning is consistent with the position of the Fermi level determined with tunneling spectroscopy for reconstructed and oxidized $In_{0.53}Ga_{0.47}As$ (001) surfaces [26,27,28]. Hence, the KFPM measurement is relevant for the assesment of a change of quantum confinement along the QD chain. We note that discrepancies exist in the literature depending on the chemistry of the surface and the techniques used to characterize the position of the Fermi level at the surface [26,29]. However, in comparison with a flat (001) surface, the QD are faceted, as seen in figure 2d, involving a higher density of surface states in the band gap which implies a stronger pinning of the Fermi level midgap.

Focusing on the variation of the CPD along the QD chain, a stronger quantum confinement with smaller QDs implies a larger band gap, delineated by the dotted bands in figure 3(g). As the energy separation between the quantized states in the valence and conduction bands also increases with the quantum confinement, the net charge in the QDs changes. Balancing the positive holes on the remaining quantized states at the top of the valence band, which are transferred from the p-type doped InP substrate across the depletion layer, modifies the surface potential. This effect leads to a reduction of the CPD contrast while the QDs get smaller, as seen in the KPFM image of figure 3(b). When plotted as a profile in figure 3(d), the CPD drops by 20 mV for the QDs with an intermediate height. This reduction reaches 26 mV for the smallest QDs. It arises from the decrease of the downward band bending, as illustrated in figure 3(g) when not only the band gap is compared between the QD and the InGaAs bulk but also the curvature of the bands.

To further estimate the change of confinement, the electronic structure of the QD chain was investigated with tunneling spectroscopy at 77 K. Figure 4 shows tunneling spectra measured on a big QD, a smaller QD and at the position of a bridge between two adjacent QDs. These structures are respectively labeled QD1, QD2 and BR1. Based on the height profiles of figure 4(c), they have lengths of 95 ± 1 nm, 78 ± 1 nm and 55 ± 1 nm, while their respective heights are 28 ± 1 nm, 25 ± 1 nm and 14 ± 1 nm. In the tunneling spectra, the valence and conduction band states are probed at negative and positive bias respectively. For the states of the InGaAs structures which are not in resonance with the states of the InP substrate, their access is made possible thanks to the tunnelling of holes from the p-type doped InP substrate at negative bias and the efficient electron-hole recombination at positive bias, as depicted in the inset of Fig. 4(a) [28].

The valence and conduction bands are separated by an apparent band gap defined as the bias range where the tunneling current reaches the experimental noise. We note that the apparent band gap may be larger than the true band gap of the different structures, consistent with previous study [18,28]. Due to the absence of doping in the InGaAs QD

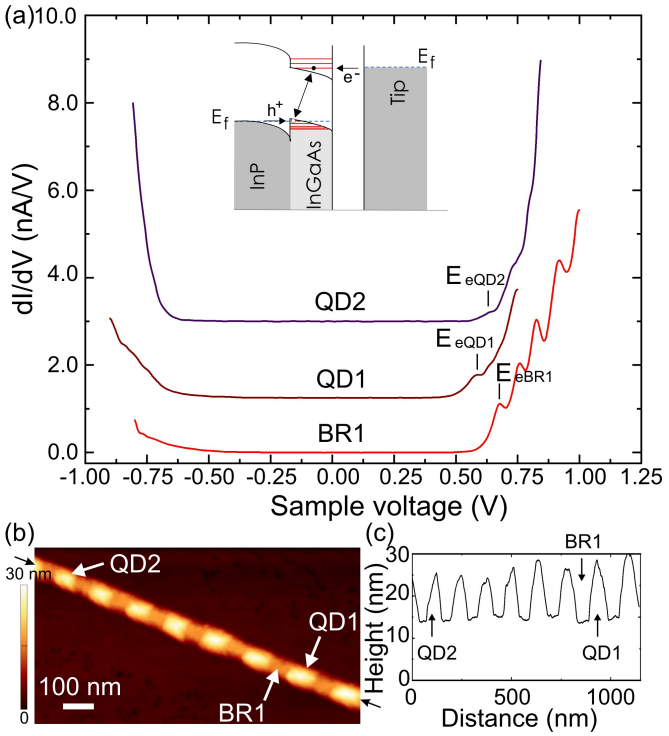

Figure 4. (a) dI/dV spectra acquired at 77 K on the QD1, QD2 and the bridge (BR1) indicated by the white arrows in the STM image shown in (b). The lowest conduction band state for each element is labelled E_e. Inset: band diagram of the tunneling junction where an electron is transferred at positive bias from the tip Fermi level E_f to E_e, and subsequently recombines with a hole supplied by the valence band of the InP substrate. Feedback parameters: (QD1) V_s = -0.9V, I_t = 210 pA; (QD2) V_s = +0.9V, I_t = 202 pA; (BR1) V_s = +1.0V, I_t = 828 pA. (c) STM height profile measured along the chain at the position indicated by the black arrows in (b).

chain and the existence of a depleted region at the InGaAs/InP interface, the potential does not fully drops across the vacuum junction, but also at the interface with the p-type doped InP substrate and to a lesser extend along the thickness of the InGaAs layer. This system resembles a capacitive model, where the InGaAs structure is weakly coupled to the two leads, the STM tip and the InP substrate respectively. Hence, the potential distribution is characterized by a lever arm, corresponding to the ratio between the capacitance of the depleted region and the sum of the capacitances of the depleted region and the vacuum junction.[30] Because the lever arm can be smaller than one, the apparent band gap is usually larger than the single particle band gap. Although the lever arm is not known, it is reasonable to assume a similar lever arm for each InGaAs structure with, at their top surface, an identical Fermi level pinning measured at zero bias. As a result, the spectral position of the conduction band states can be compared between the three InGaAs structures.

The measurement of the lowest peak in the conduction band for QD1 and QD2 yields a separation of 50 mV

between E_{eQD1} and E_{eQD2} consistent with a smaller QD2 and thus a stronger confinement. The quantum confinement further increases in BR1, as a difference of 90 mV is measured between E_{eBR1} and E_{eQD1}. It is predominantly caused by the height difference between BR1 and QD1. Such a stronger confinement in the bridge is highlighted by the three additional peaks that are clearly observed at higher bias. As the bridge corresponds to the initial NW, these peaks are associated with delocalized states along the chain. Hence, they should also exist in the QDs, which stand on the NW. But their spatial depth makes the transmission probability between the tip states and the QD states much weaker, preventing their detection in the spectra.

4. Conclusion

In conclusion, we have shown that $In_{0.53}Ga_{0.47}As$ quantum dot chains can be obtained with a twofold selective area growth. By developing a device layout compatible with scanning probe microscopies, individual chains were characterized and exhibited a change of quantum confinement with the dot size. As our approach can be further improved by reducing the NW dimensions and by integrating low effective mass semiconductor materials (InAs or InSb), QD lattices with stronger quantum confinement effects are achievable. Moreover, the flexibility and precision ensured by multiple fold selective area molecular beam epitaxy opens the door to the creation of more complex QD architectures such as the linear Su-Schrieffer-Heeger chains with staggering patterns, and the two-dimensional Lieb or honeycomb lattices.

Acknowledgements

This study was financially supported by the French National Research agency (INSPIRING project ANR-21-CE09-0026-01), the IEMN PCMP-PCP and CMNF platforms of the French Technological Network RENATECH, and the Région Hauts de France. The authors thank X. Wallart for fruitful discussions.

References

[1] Reimann S M and Manninen M 2002 *Rev. Mod. Phys.* **74** 1283
[2] Hanson R, Kouwenhoven L P, Petta J R, Tarucha S and Vandersypen L M 2007 *Rev. Mod. Phys.* **79** 1217
[3] Zwolak J P and Taylor J M 2023 *Rev. Mod. Phys.* **95** 011006
[4] Hensgens T, Fujita T, Janssen L, Li X, Van Diepen C J, Reichl C, Wegscheider W, Das Sarma S and Vandersypen L M, 2017 *Nature* **548** 70-73
[5] Hendrickx N W, Lawrie W I, Russ M, van Riggelen F, de Snoo S L, Schouten R N, Sammak A, Scappucci G and Veldhorst M 2021 *Nature* **591** 580-585
[6] Mortemousque P A, Chanrion E, Jadot B, Flentje H, Ludwig A, Wieck A D, Urdampilleta M, Bäuerle C and Meunier T. 2021 *Nat. Nanotechnol.* **16** 296-301
[7]Borsoi F, Hendrickx N W, John V, Meyer M, Motz S, Van Riggelen F, Sammak A, de Snoo S L, Scappucci G and Veldhorst M 2024 *Nat. Nanotechnol.* **19** 21-27
[8]Lee J S, Sugisaki M, Ren H W, Sugou S and Masumoto Y2000 *Phys. E: Low-Dimens. Syst. Nanostructures* **7** 303-307
[9]Wang Z M, Holmes K, Mazur Y I and Salamo G J 2004 *Appl. Phys. Lett.* **84** 1931-1933
[10]Post L C, Xu T, Franchina Vergel N F, Tadjine A, Lambert Y, Vaurette F, Yarekha D, Desplanque L, Stiévenard D, Wallart X, Grandidier B, Delerue C and Vanmaekelbergh D 2019 *Nanotechnology* **30** 155301
[11]Franchina Vergel N A, Post L C, Sciacca D, Berthe M, Vaurette F, Lambert Y, Yarekha D, Troadec D, Coinon C, Fleury G, Patriarche G, Xu T, Desplanque L, Wallart X, Vanmaekelbergh D, Delerue C and Grandidier B 2020 *Nano Lett.* **21** 680-685
[12]Gooth J, Borg M, Schmid H, Schaller V, Wirths S, Moselund K, Luisier M, Karg S and Riel H 2017 *Nano Lett.* **17**, 2596 - 2602
[13]Friedl M, Cerveny K, Weigele P, Tütüncüoglu G, Martí-Sánchez S, Huang C, Patlatiuk T, Potts H, Sun Z, Hill M O, Güniat L, Kim W, Zamani M, Dubrovskii V G, Arbiol J, Lauhon L J, Zumbühl D M and Fontcuberta i Morral A 2018 *Nano Lett.* **18** 2666 - 2671
[14]Vaitiekėnas S, Whiticar A M, Deng M-T, Krizek F, Sestoft J E, Palmstrøm C J, Martí-Sánchez S, Arbiol J, Krogstrup P, Casparis L and Marcus C M 2018 *Phys. Rev. Lett.* **121** 147701
[15]Aseev P, Fursina A, Boekhout F, Krizek F, Sestoft J E, Borsoi F, Heedt S, Wang G, Binci L, Martí-Sánchez S, Swoboda T, Koops R, Uccelli E, Arbiol J, Krogstrup P, Kouwenhoven L P and Caroff P 2019 *Nano Lett.* **19**, 218 - 227
[16]Op het Veld R L M, Xu D, Schaller V, Verheijen M A, Peters S M E, Jung J, Tong C, Wang Q, de Moor M W A, Hesselmann B, Vermeulen K, Bommer J D S, Lee J S, Sarikov A, Pendharkar M, Marzegalli A, Koelling S, Kouwenhoven LP, Miglio L, Palmstrøm C J, Zhang H and Bakkers E P A M 2020 *Commun. Phys.* **3**, 59
[17]Bucamp A, Coinon C, Codron J L, Troadec D, Wallart X and Desplanque L 2019 *J. Cryst. Growth* **512** 11-15
[18]Peric N, Durand C, Berthe M, Lu Y, N'konou K, Coratger R, Lefebvre I, Ebert Ph, Biadala L, Desplanque L, Wallart X and Grandidier B 2022 *Appl. Phys. Lett.* **121** 192104
[19]Bucamp A, Coinon C, Troadec D, Lepilliet S, Patriarche G, Wallart X and Desplanque L 2020 *Nano Research* **13** 61-66
[20]Álvarez A D, Peric N, Franchina Vergel N A, Nys J P, Berthe M, Patriarche G, Harmand J-C, Caroff P, Plissard S, Ebert Ph, Xu T and Grandidier B 2019 *Nanotechnology* **30** 324002
[21]Yamauchi T, Tabuchi M and Nakamura A *Appl. Phys. Lett.* **84** 3834-3836
[22] Moran T J, Suzuki K, Hosokura T, Khaetskii A and Huey B D 2021 J. Am. Ceram. Soc. **104** 5157-5167
[23]Fischer T E *Phys. Rev.* 1966 **142** 519
[24]Lau W M, Sodhi R N S and Ingrey S 1988 *Appl. Phys. Lett.* **52** 386 - 388
[25]Biadala L, Peng W, Lambert Y, Kim J H, Canneson D, Houppe A, Berthe M, Troadec D, Deresmes D, Patriarche G, Xu T, Pi X, Wallart X, Delerue C, Bayer M, Xu J and Grandidier B 2019 *ACS Nano* **13** 1961-1967
[26]Melitz W, Shen J, Lee S, Lee J S, Kummel A C, Droopad R and Yu E T 2010 *J. Appl. Phys.* **108** 023711
[27] Minkevičius L, Tamošiūnas V, Kojelis M, Žąsinas E, Bukauskas V, Šetkus A, Butkutė R, Kašalynas I and Valušis G 2017 *J. Infrared Millim. Terahertz Waves* **38** 689-707

[28]Franchina Vergel N A, Tadjine A, Notot V, Mohr M, N'Guissan A K, Coinon C, Dzagli M M, Girard J-C, Rodary G, Desplanque L, Berndt R, Stiévenard D, Wallart X, Delerue C and Grandidier B 2019 *Phys. Rev. Mater.* **3** 094604

[29]Taoka N, Yokoyama M, Hyeon Kim S, Suzuki R, Lee S, Iida R, Hoshii T, Jevasuwan W, Maeda T, Yasuda T, Ichikawa O, Fukuhara N, Hata M, Takenaka M and Takagi S 2013 *Appl. Phys. Lett.* **103** 143509

[30]Nguyen T H, Habinshuti J, Justo Y, Gomes R, Mahieu G, Godey S, Nys J P, Carrillo S, Hens Z, Robbe O, Turrell S and Grandidier B 2011 *Phys. Rev. B* **84** 195133